ACS central science

http://pubs.acs.org/journal/acscii

Research Article

# Revealing a Hidden Intermediate of Rotatory Catalysis with X-ray Crystallography and Molecular Simulations

Mrinal Shekhar,[#] Chitrak Gupta,[#] Kano Suzuki,[#] Chun Kit Chan, Takeshi Murata,* and Abhishek Singharoy*

Cite This: *ACS Cent. Sci.* 2022, 8, 915–925

Read Online

ACCESS | Metrics & More | Article Recommendations | Supporting Information

**ABSTRACT:** The mechanism of rotatory catalysis in ATP-hydrolyzing molecular motors remains an unresolved puzzle in biological energy transfer. Notwithstanding the wealth of available biochemical and structural information inferred from years of experiments, knowledge on how the coupling between the chemical and mechanical steps within motors enforces directional rotatory movements remains fragmentary. Even more contentious is to pinpoint the rate-limiting step of a multistep rotation process. Here, using vacuolar or $V_1$-type hexameric ATPase as an exemplary rotational motor, we present a model of the complete 4-step conformational cycle involved in rotatory catalysis. First, using X-ray crystallography, a new intermediate or "dwell" is identified, which enables the release of an inorganic phosphate (or $P_i$) after ATP hydrolysis. Using molecular dynamics simulations, this new dwell is placed in a sequence with three other crystal structures to derive a putative cyclic rotation path. Free-energy simulations are employed to estimate the rate of the hexameric protein transformations and delineate allosteric effects that allow new reactant ATP entry only after hydrolysis product exit. An analysis of transfer entropy brings to light how the side-chain-level interactions transcend into larger-scale reorganizations, highlighting the role of the ubiquitous arginine-finger residues in coupling chemical and mechanical information. An inspection of all known rates encompassing the 4-step rotation mechanism implicates the overcoming of the ADP interactions with $V_1$-ATPase to be the rate-limiting step of motor action.

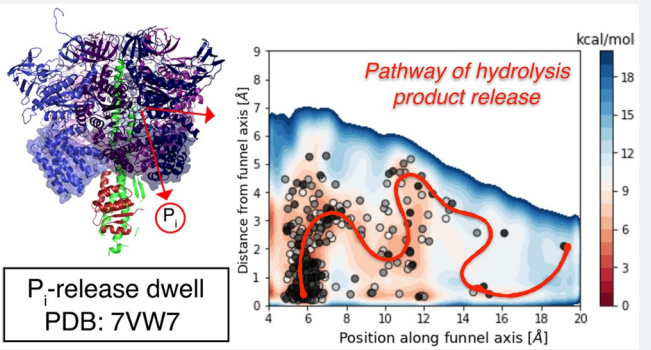


## INTRODUCTION

V-type ATPase from *Enterococcus hirae* is a prototypical ATP-driven rotary molecular motor. It harnesses energy from ATP hydrolysis to pump ions across biological membranes.[1] Crystallographic studies reveal that V-ATPases possess an overall three-dimensional structure, composed of a hydrophilic domain ($V_1$) and a membrane-embedded, ion-transporting domain ($V_o$) connected by a central and peripheral stalk(s).[2−8] The $V_1$ domain consists of an $A_3B_3$ ring (composed of 3 repeats of A and B subunits) and a central stalk (Figure 1). Ubiquitous to all rotary ATPases, including the famous $F_1$-ATP synthase, $V_1$-ATPases partake in "rotatory catalysis",[1] a catalytic mechanism wherein the chemical reactions, e.g., ATP hydrolysis, occur through conformational rotation of the $A_3B_3$ ring and physical rotation of the central stalk.[2,3]

The rotatory catalysis mechanism was originally proposed by Boyer in the 1980s,[9] and Walker and colleagues spent the following two decades finding key structural intermediates (popularly known as *dwell* states) along the ATP hydrolysis pathway,[10−15] which is also supported by Senior's mutational and biochemical analysis of the motor.[16] However, molecular details of a contiguous reaction pathway linking the individual dwell states are being uncovered only recently by using a combination of fast single-molecule experiments[17] and multi-scale molecular dynamics simulations.[18−20] Contributing to this body of information, we have determined the crystal structures of the so-called "catalytic dwell", "ATP-binding dwell", and "ADP-release dwell" of the motor and have proposed the $V_1$-ATPase rotational mechanism model based on the crystal structures and molecular simulations.[21,22]

Illustrated in Figure S1, our proposed multisite catalytic mechanism includes the following: (i) ATP hydrolysis into ADP and inorganic phosphate (or $P_i$) in the *tight* AB domains of the $A_3B_3$ ring within the catalytic dwell [PDB: 3VR6][2] is accompanied by a loosening of the *tight* AB interface and straightening of the DF stalk subunit. (ii) After the hydrolysis reaction, the ADP remains bound to the *tight* interface, and the

**Received:** January 3, 2022
**Published:** June 14, 2022

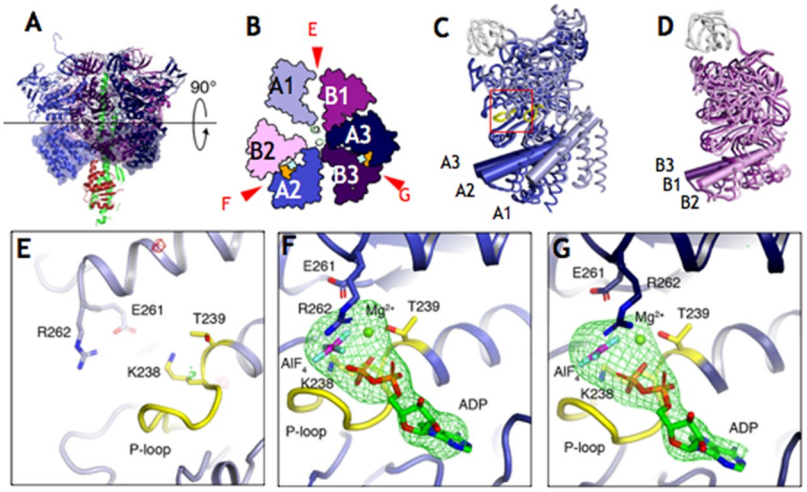


**Figure 1.** Structure of the $2_{(ADP\cdot AlF4)}V_1$-bound $V_1$ complex. (A) Side view of $2_{(ADP\cdot AlF4)}V_1$. (B) Top view of the C-terminal domain (shown in panel A at the transparent surface) of $2_{(ADP\cdot AlF4)}V_1$ from the cytoplasmic side. Red arrows indicate the nucleotide-binding sites. The bound ADP and $AlF_4^-$ molecules are shown in a space-filling representation and colored orange and cyan, respectively. Superimposed structure at the N-terminal $\beta$-barrel region (white) of three structures of A subunits (C) and B subunits (D) in $2_{(ADP\cdot AlF4)}V_1$. A subunits are colored light blue (A1 or $A^e$), dark blue (A2 or $A^b$), and darker blue (A3 or $A^t$) in order of openness. Similarly for the B subunits: dark purple (B1 or $B^e$), light purple (B2 or $B^b$), and darker purple (B3 or $B^t$). The P-loops are shown in yellow. (E–G) Magnified view of the nucleotide-binding sites of $2_{(ADP\cdot AlF4)}V_1$, corresponding to the red box of panel C. The positions of the nucleotide-binding sites correspond to the symbol written in panel B. The |Fo| − |Fc| maps calculated without ADP:$Mg^{2+}$ and aluminum fluoride molecules at the binding pockets contoured at 4.0 sigma are shown in red (negative) and green (positive).

neighboring *empty* AB domains open up to become *bindable* for accepting a new ATP in the pocket, transforming to the ATP-binding dwell [PDB: 5KNB].[3] (iii) The new ATP binds to this bindable site making it *half-closed*, and the motor transforms to the ADP-release dwell [PDB: 5KNC].[3] (iv) Following ADP release, the DF stalk undergoes a deformation and subsequent 120° rotation, so the symmetry of the system is reset back to the catalytic dwell [PDB: 3VR6], completing one cycle of rotatory catalysis.[3]

The hydrolysis-product release step is implicated as rate-determining in other related motors, such as the hexameric helicases[23] and even in F-type ATPases.[18] However, the crystallographic structures of $V_1$-ATPase determined so far did not include states immediately after ATP hydrolysis and before $P_i$ release, keeping details of this key step of the catalytic cycle elusive. In this study, we report the crystal structure of *E. hirae* $V_1$ ATPase ($EhV_1$), in which the aluminum fluoride (or $AlF_4^-$) and ADP molecules are bound at two nucleotide-binding sites. It has been discussed that the aluminum fluoride and ADP-bound structure mimics the transition state of ATP hydrolysis. Analogous to the structures of myosin,[24] $F_1$-ATPase,[12] and other ATPases that have been obtained with aluminum fluoride bound, we seek the posthydrolysis mechanism of the $V_1$ motor action. Compared with the crystal structure in the catalytic dwell state that has an ATP-bound tight AB pair, we find the model with an ADP·$AlF_4^-$-bound AB pair to be marginally open. This AB interface is open enough to allow $P_i$ release but not as wide to allow release of the ADP. We therefore interpret that the ADP·$AlF_4^-$-bound ATPase structure corresponds to a state of waiting for $P_i$ release following ATP hydrolysis and label this state as the "$P_i$-release dwell". Starting from the crystal structure of the catalytic dwell, we performed molecular dynamics and free-energy simulations to model the $P_i$ release pathway following ATP hydrolysis. An allosteric mechanism is described that connects product release from the tight pocket with increased ATP affinity in the neighboring bindable pocket. This way, using simulations, we place the $P_i$-release dwell in the sequence of events lining the overall rotatory catalysis mechanism in $EhV_1$ and complete the first molecular description of the entire conformational cycle joining four X-ray crystallographically determined intermediates. A kinetic analysis of the product release mechanism offers insights on the rate-determining step of molecular motor action.

## RESULTS

In what follows, first, the $EhV_1$ with ADP and aluminum fluoride is crystallized, and the 3D-structure of the ADP·$AlF_4^-$-bound $V_1$ is determined employing X-ray crystallography. Second, local and global structural differences between this ADP·$AlF_4^-$-bound $V_1$ model and that from the ATP-binding catalytic dwell state are computed to ascertain the location of the $P_i$-release dwell along the rotatory catalysis cycle (Figure 2). Third, molecular dynamics simulations reveal a mechanism of $P_i$ release, which couples the $P_i$-release dwell with the following ATP-binding and ADP-release dwells. Finally, noting that the path ensuing from this ATP-binding dwell to ADP-release dwell resetting back to another catalytic dwell is already established in our previous studies,[22,25,26] a complete model for rotatory catalysis in V-type ATPases is accomplished.

**Crystallization of $V_1$-ATPase with ADP and Aluminum Fluoride Reveals a New Intermediate.** It has been reported that the ATPase activity of bovine mitochondrial $F_1$-ATPase is inhibited in the presence of ADP and aluminum fluoride.[12] In this study, we purified $EhV_1$ in the presence of ADP and $AlF_4^-$, analogous to the case of the bovine $F_1$-ATPase (see the Methods section). The ATP hydrolysis activity of the purified $EhV_1$ was not observed, suggesting that the $EhV_1$ was indeed inhibited by binding of ADP·$AlF_4^-$ in the nucleotide-binding site(s). We crystallized the inhibited $EhV_1$ and obtained a crystal structure at 3.8 Å resolution on an *R* factor of 22.7% and a free *R* factor of 26.6% (Table 1). We note,


https://doi.org/10.1021/acscentsci.1c01599
ACS Cent. Sci. 2022, 8, 915–925

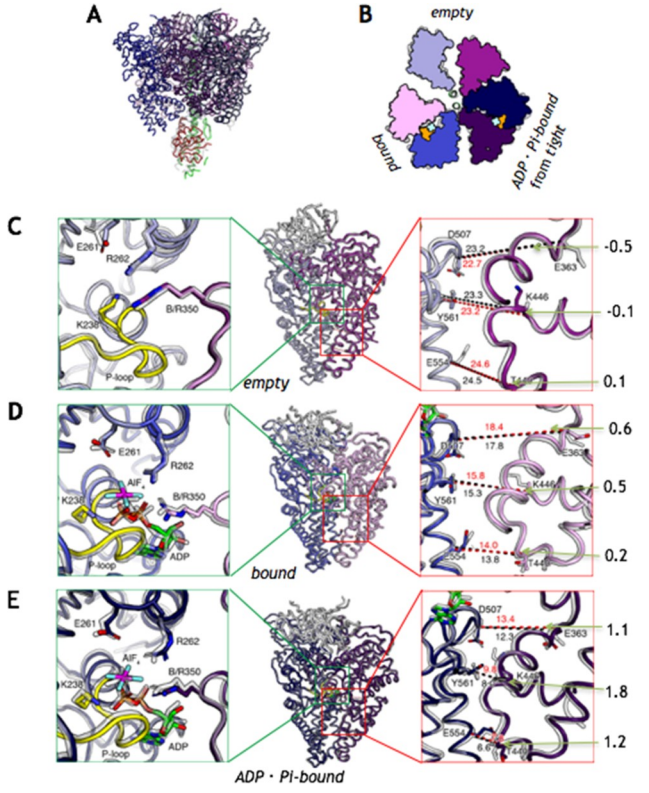


**Figure 2.** Comparison of the structures of 2 ADP·$AlF_4^-$-bound and 2 AMP·PNP-bound $V_1$complexes. (A, B) The structures of $2_{(ADP·AlF4)}V_1$ (colored) are superposed on the AMP·PNP-"*bound*" or $2_{(AMP·PNP)}V_1$ conformations (shown in gray). (A) Side view and (B) top view of the C-terminal domain from the cytoplasmic side. The bound $AlF_4^-$ and ADP molecules are shown in space-filling representation and colored cyan and orange, respectively. (C−E) The "*empty*" (C), "*bound*" (D), and "*ADP·$P_i$-bound*" (E) forms in $2_{(ADP·AlF4)}V_1$ (colored) are superimposed on those of $2_{(AMP·PNP)}V_1$ (shown in transparent gray) at A subunits (residues 67−593). (left) Magnified views of the nucleotide binding sites, corresponding to the green box of middle panels. (middle) Side views of AB pairs. (right) Magnified views of the interface of C-terminal domains, corresponding to the red box of the middle panels. Red ($2_{(ADP·AlF4)}V_1$) and black ($2_{(AMP·PNP)}V_1$) dotted lines indicate the distances (Å) between $C_\alpha$ atoms. The numbers outside the panel represent the value of the lengths of the red dotted lines minus the lengths of the black dotted lines.

**Table 1. Data Collection and Refinement Statistics**

| | |
|---|---|
| Data Collection | |
| space group | $P2_12_12_1$ |
| cell dimensions: *a*, *b*, *c* (Å) | 127.7, 128.9, 231.6 |
| cell dimensions: *α*, *β*, *γ* (deg) | 90.0, 90.0, 90.0 |
| resolution (Å) | 46.13−3.82 (4.05−3.82) |
| $R_{merge}$ | 0.172 (0.953) |
| $I/\sigma I$ | 7.61 (1.54) |
| completeness (%) | 99.5 (99.0) |
| redundancy | 3.9 (3.8) |
| Refinement | |
| $R_{work}/R_{free}$ (%) | 22.69/26.56 |
| R.m.s. deviations: bond lengths (Å) | 0.003 |
| R.m.s. deviations: bond angles (deg) | 0.509 |
| Ramachandran plot statistics (%): favored regions | 97.8 |
| Ramachandran plot statistics (%): allowed regions | 2.1 |
| Ramachandran plot statistics (%): outliers | 0.0 |

however, that although the number of dwell states in $EhV_1$ and mammalian $F_1$ appears to be the same, these $V_1$ and $F_1$ motors show clear differences in the release order of cleavage products, rotational arrest points, dynamics, and conformational changes.[3] Thus, the ADP·$AlF_4^-$-inhibited $V_1$ and $F_1$ motors need not yield similar functional states. A physical interpretation of the stationary $AlF_4^-$-inhibited $V_1$ structure is hence derived by comparison with only the other known crystallographic V-type models (and not the F-type ones), followed by computer simulations.

**Structure of the $V_1$ Complex with ADP and Aluminum Fluoride.** The obtained crystal structure was composed of a hexagonally arranged $A_3B_3$ complex and a central axis DF complex as the previously reported structures of $EhV_1$[2] (Figure 1A,B). We superimposed the N-terminal *β*-barrel domain of the three A or B subunits to evaluate the conformational differences in the $EhV_1$ complex because the *β*-barrel domain should be fixed to form an alternatively arranged ring[2] (Figure 1C,D). All A and B subunits showed different conformations, suggesting that this inhibited $EhV_1$ is also formed in an asymmetric structure as the other published structures of $EhV_1$. Three nucleotide-binding sites are at the interface between the A and B subunits. Two strong electron density peaks were observed in two nucleotide-binding sites (Figure 1E−G). ADP:$Mg^{2+}$ and $AlF_4^-$ molecules were fitted well into both density peaks. Therefore, we denote this structure as $2_{(ADP·AlF4)}V_1$ from here on.

Structural differences between 2 ADP·$AlF_4^-$-bound and 2 AMP·PNP-bound $V_1$ complexes highlight molecular conformations before and after $P_i$ release. We previously reported that 2 AMP-PNP-bound $EhV_1$ (denoted as $2_{(AMP·PNP)}V_1$), corresponding to the catalytic dwell state during rotatory catalysis, consists of three different conformation AB pairs: *empty* (site that cannot bind nucleotides), *bound* (site that can bind ATP), and *tight* (site waiting for ATP hydrolysis). The structures of $2_{(ADP·AlF4)}V_1$ and $2_{(AMP·PNP)}V_1$ are compared in Figure 2. The overall structure of $2_{(ADP·AlF4)}V_1$ was very similar to that of $bV_1$ (root-mean-square deviation: RMSD = 0.78 Å) (Figure 2A, B). In particular, the *empty* site of the $2_{(AMP·PNP)}V_1$ is very similar to the AB pair with no nucleotide of $2_{(ADP·AlF4)}V_1$ (RMSD = 0.51 Å): these nucleotide-binding sites are almost identical, and the distances between the C-terminal domains of the AB pairs are also very similar (Figure 2C). The *bound* site of $2_{(AMP·PNP)}V_1$ is also similar to an AB pair which binds ADP:$Mg^{2+}$ and $AlF_4^-$ in $2_{(ADP·AlF4)}V_1$ (RMSD = 0.51 Å): these nucleotide-binding sites bind different substrates, but the structures of the binding sites and the distances between the AB pairs are very similar (Figure 2D).

In contrast, the remaining third AB pair-bound ADP:$Mg^{2+}$ and $AlF_4^-$ molecules of $2_{(ADP·AlF4)}V_1$ show prominent local differences when compared with the *tight* site-bound AMP·PNP:$Mg^{2+}$ of $2_{(AMP·PNP)}V_1$, although the overall RMSD between these two AB pairs is 0.62 Å. Illustrated in Figure 2E, we find that the conformations of the conserved residues of E261 and R262 of A subunit and the Arg-finger (R350 in B subunit) are deviated by 1.1−1.8 Å, which is probably induced by binding of the $AlF_4^-$ molecule instead of the gamma-phosphate of AMP·PNP; such conformational differences were much lesser (between 0.1 and 0.6 Å) with the *empty* and *bound* sites of the $2_{(ADP·AlF4)}V_1$ structure relative to $2_{(AMP·PNP)}V_1$, as seen in Figure 2C,D. Furthermore, the C-terminal domain of the AB pair shows a slightly open conformation that may allow $P_i$ release but not as wide to allow the release of the ADP


https://doi.org/10.1021/acscentsci.1c01599
ACS Cent. Sci. 2022, 8, 915−925

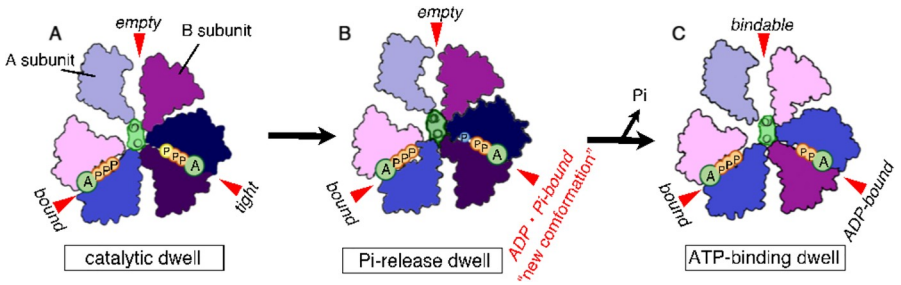


**Figure 3.** Proposed model of the rotation mechanism of *E. hirae* $V_1$-ATPase. (A–C) The structure models are based on the crystal structures of catalytic dwell ($2_{(AMP\cdot PNP)}V_1$ in panel A), $P_i$-release dwell ($2_{(ADP\cdot AlF4)}V_1$ in panel B), and ATP-binding dwell ($2_{ADP}V_1$ in panel C). The ATP indicated with a yellow terminal $P_i$ is committed to hydrolysis.

(Figure 2E). From these findings, we designated the AB pair, which was more open than the *tight*, as *ADP·$P_i$-bound* form and interpreted that the structure corresponds to the state of waiting for $P_i$ release (denoted as "$P_i$-release dwell") following ATP hydrolysis.

**$P_i$-Release Dwell—A New Step in the Rotational Mechanism.** Here, we integrate the $P_i$-release dwell into the rotational mechanism model for $V_1$-ATPase based on all available crystal structures (see Figure S1 and Figure 3): The rotation mechanism model starts with a catalytic dwell in which $V_1$-ATPase binds two ATP molecules at the *bound* and *tight* sites. Since the Arg-finger residue R350 in the *tight* site is in close proximity to the ATP gamma-phosphate, this ATP is waiting for hydrolysis. The cycle begins with the hydrolysis of this ATP (Figure 3A). The ATP in the *tight* site is hydrolyzed and produces ADP and $P_i$, which induce the conformational change to the *ADP·$P_i$-bound* form, waiting for $P_i$ release from the binding site; this state represents the $P_i$-release dwell in Figure 3B. The product, $P_i$, is released from the slightly open conformation of this *ADP·$P_i$-bound* site. Then, the resulting *ADP-bound* ATPase, complexing with just one ADP, is created. Herein, a conformational transition of the *empty* site (120° apart from the ADP-bound site) renders it to a *bindable* form. The *empty* site has a low affinity to bind nucleotides;[2] however, due to this conformational change, a new ATP becomes accessible to the *bindable* form. This structure is, therefore, referred to as the "ATP-binding dwell", waiting for new ATP binding (Figure 3C) to subsequently enable the rotation of the central stalk (Figure S1).[8] In the following, we evaluate the proposed model with molecular dynamics or MD simulations.

**Transition from Catalytic Dwell to $P_i$-Release Dwell Is Spontaneous after ATP Hydrolysis.** We replaced the AMP·PNP in the *tight* pocket of the catalytic dwell (3VR6) model with an ADP·$P_i$ ($P_i$ modeled as $H_2PO_4^-$) and simulated the system in explicit solvent using all-atom MD for 500 ns. Each simulation was replicated thrice, wherein the *empty* site was left nucleotide-free and the *bound* site included in ATP (list of simulations provided in Table S1). Similar simulations were also performed with the *tight* AMP·PNP replaced by an ATP.[25] To construct these simulation models, the ATP, ADP, and AMP are aligned based on the geometry of the adenine ring and the first phosphate moiety.[26]

As illustrated in Figure 4A, prior to hydrolysis, the ATP remains bound to the G235, G237, K238, R262, and F425 residues of the A subunit of the *tight* pocket and the Arg-finger R350 residue of the B subunit (denoted $A^t$ and $B^t$, and a similar site-wise nomenclature is followed for all other AB pairs). Consequently, the correlated dynamics of the $A^t$ and $B^t$ subunits is regulated by the interface-bound ATP (Figure 4C).

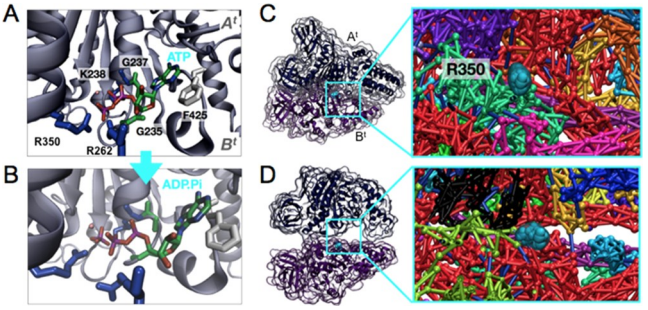


**Figure 4.** ATP hydrolysis breaks the dynamic coupling between A- and B-subunits. (A) ATP is bound to the binding pocket, formed by G235, G237, K238, R262, and F425 of the A-subunit and R350 of the B-subunit, prior to hydrolysis. In this state, the $A^t$- and $B^t$-subunits are tightly coupled due to the presence of the ATP. (B) Upon hydrolysis and prior to release of the inorganic phosphate ($P_i$), the ADP and $P_i$ moieties interact primarily with the A- and B-subunits, breaking the tight coupling seen in panel A. (C) Network model showing correlated movements between the A- and B-subunits before hydrolysis, with R350 of the B-subunit highlighted in blue. Tight binding of the subunits gives rise to a strong network. (D) Correlated movements between the A- and B-subunits after hydrolysis, with R350 of the B-subunit highlighted in blue. Breakage of the tight coupling between the subunits results in a weakly coupled network.

On breaking the covalent bond to the terminal phosphate, the ADP stays connected to the A subunit, while the $P_i$ interacts primarily with the Arg-finger of the B-subunit. Thus, the communication across the bound ATP is lost (Figure 4D), resulting in a looser ADP·$P_i$-bound AB interface. This looseness of the ADP·$P_i$-bound interface is reflected in elevated fluctuations of the $A^t$ subunit posthydrolysis (Figure S2).

The RMSD between the simulated ADP·$P_i$-bound models and the $P_i$-release dwell X-ray structure (i.e., the $2_{(ADP\cdot AlF4)}V_1$ model) is peaked ~1.4 Å, which is lesser than the 1.7 Å RMSD between the catalytic dwell (i.e., the $2_{AMP\cdot PNP}V_1$ model) model (PDB: 3VR6) and our simulated ADP·$P_i$-bound model. Though small, the differences between the ADP·$P_i$-bound model and the catalytic dwell model are statistically significant (Figure S3). This trend is amplified when we compare RMSD values between the simulated ADP·$P_i$-bound model with those from the ATP-binding dwell following the release of $P_i$ (PDB: 5KNB). Our simulated ADP·$P_i$-bound model is found to be deviated from the 5KNB model by 2.3 Å, which is more than its deviation from the catalytic dwell seen in Figure S3. Noting that RMSD between the *tight* forms of 3VR6 and 5KNB is ~3 Å; we find that the $V_1$ models with ADP·$P_i$-bound to $A^tB^t$ are close to yet distinct from the structure of the catalytic dwell


https://doi.org/10.1021/acscentsci.1c01599
ACS Cent. Sci. 2022, 8, 915–925

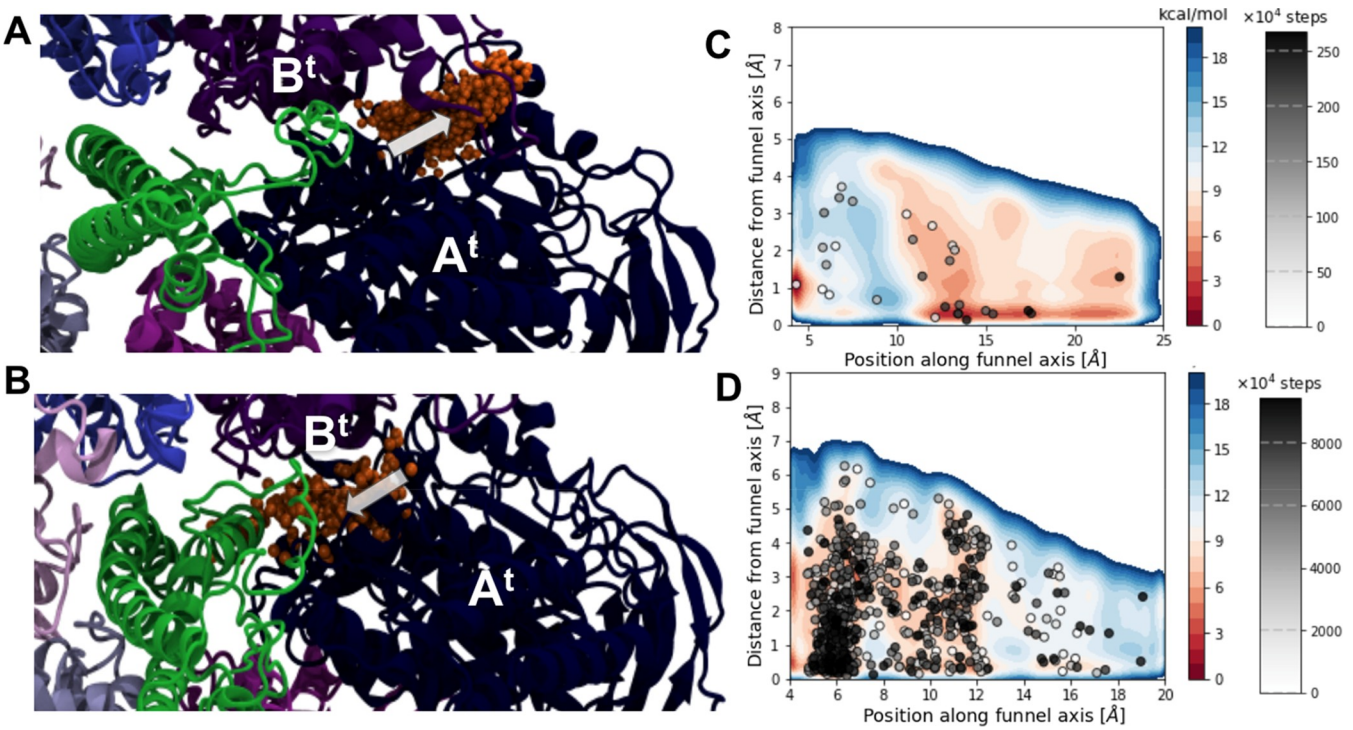


**Figure 5.** Pathways of $P_i$ release. The two simulated pathways for phosphate release are either (A) *outward* (away from the stalk) or (B) *inward* (toward the stalk). The first event of phosphate release captured using funnel metadynamics is shown; $P_i$ molecules are shown as orange spheres with the white arrow depicting the direction of egress. The free energy for the phosphate release computed by funnel metadynamics along the funnel and orthogonal axes is shown for the (C) outward pathway and (D) inward pathway. The outward $P_i$-release pathway is energetically less expensive. In the vicinity of the binding pocket, the inward pathway is more constrained and encompasses higher barriers following disengagement of $P_i$ from the pocket. Exemplary traces of a diffusive particle on these surfaces determined using BD simulations reveal that traversal of the inward pathway is ∼10-fold slower; BD time steps for probing the inner pathway are 1 ps, and those for the outer are 3 ps, as the former is found to be more rugged (see Figure S7).

and are also deviated from the ATP-binding dwell, thus justifying its own dwell state.

MD simulations of the $V_1$ motor after ATP hydrolysis therefore spontaneously deforms the structure from the catalytic dwell to the ADP·$AlF_4^-$-bound model, suggesting that, indeed, the crystal structure represents a state following ATP hydrolysis but preceding product release. The simulated ADP·$P_i$-bound model also possesses a remarkable similarity with structures from our previous string simulations,[25] wherein we found that the presence of ADP·$P_i$ in the $A^tB^t$ pocket entraps the $V_1$ rotor in a deep energy minimum and inhibits further rotation of the central stalk (Figure S4) prior to product release. Altogether, the similarity between the ADP·$P_i$-bound structures derived from the current set of MD simulations, the ones from our previous string simulations showing rotational inhibition, and the ADP·$AlF_4^-$-bound X-ray model, as well as their common difference from the ATP-bound $A^tB^t$ (in catalytic dwell) and ADP-bound $A^tB^t$ (in ATP-binding dwell), suggest the identification of a new $P_i$-release dwell.

It is worth noting that the MD simulations began with a model of the catalytic dwell, namely, 3VR6 (2.6 Å resolution), and arrived at models similar to the crystal structure of the $P_i$-release dwell. This computational result suggests, on one hand, a minimal impact of initial model bias on our inferences, while on the other hand, biological relevance of the $2_{AMP\cdot PNP}V_1$ model despite its 3.8 Å resolution.

**Transition from $P_i$-Release Dwell to ATP-Binding Dwell Involves Two Different Pathways.** If the hydrolysis product remains in the binding pocket, the rotation of the central stalk is hindered, and the motor is inhibited.[27] Thus, the next step after hydrolysis is considered to be the release of the ADP and $P_i$ products, which is suggested as the rate-determining bottleneck of the rotatory cycle in V-type as well as the more ubiquitous F-type ATPase motors.[28] Interaction energy analysis from the MD simulations revealed that the protonated inorganic phosphate has the weakest interaction with the $A^tB^t$ protein pocket, while ADP has much stronger electrostatic interactions with this pocket (Figure S5). Building on this initial insight, we performed 512 ns of replica exchange with solute tempering or REST2 simulation using 16 replicas (see the Methods section). This enhanced sampling simulation brought to light some initial stages of the product release, wherein the $P_i$ to ADP distance increased from 4 to 8 Å; however, a complete detachment of $P_i$ was not observed due to the finite time scale of the computation (Figure S6).

To determine a mechanism of product release, we therefore resorted to well-tempered Funnel metadynamics simulations.[29] A vector suggesting the direction of $P_i$ release was already identified in the REST2 simulations (arrow shown in Figure 5). Two 0.4 and 2 $\mu$s metadynamics simulations were performed, one biased toward the central stalk akin to the REST2 results, denoted the *inward* direction, and another biased in the opposite *outward* direction. The outward pathway led to complete detachment of the $P_i$ and its release in the solvent, while along the inward path, the $P_i$ did detach from the binding pocket but found a transient secondary site close to the central stalk. After the $P_i$-release from the outward


https://doi.org/10.1021/acscentsci.1c01599
ACS Cent. Sci. 2022, 8, 915−925

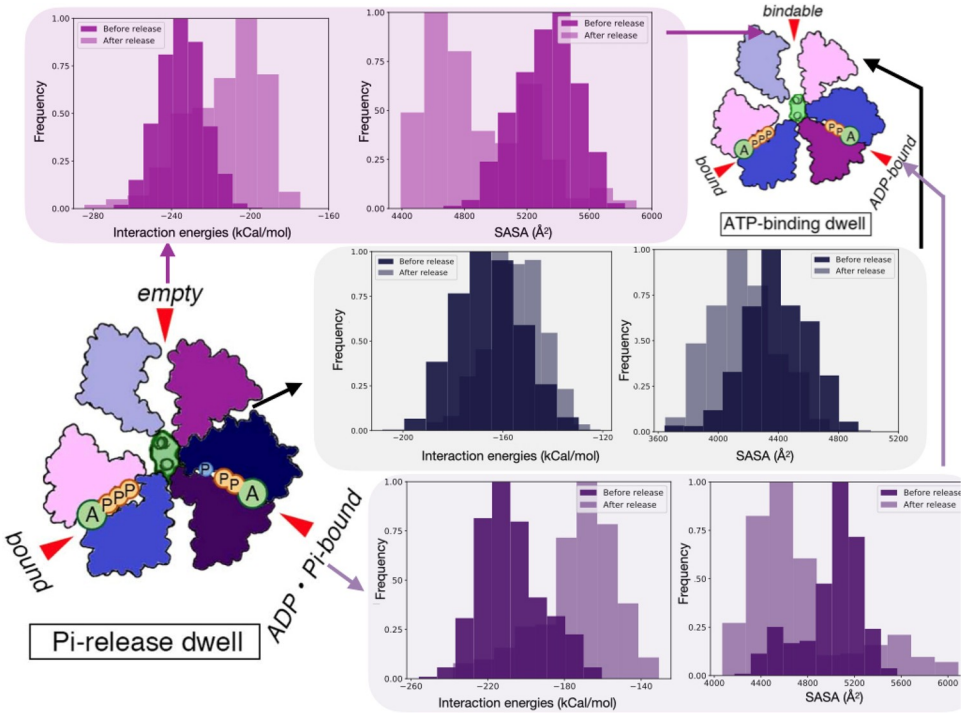


**Figure 6.** Interface energy analysis. Upon $P_i$ release, interaction energy reduces (becomes less negative) between the stalk and subunit $A^eB^e$ (top panel, left), $B^eA^t$ (middle panel, left), and $A^tB^t$ (bottom panel, left). Concomitantly, the solvent-accessible surface area (SASA) of the empty pocket (top panel, right), non-nucleotide binding pocket (middle panel, right), and ADP·$P_i$-bound pocket (bottom panel, right) undergoes an increase. This increase in SASA of the empty pocket allows it to accept a new ATP molecule to reset the rotatory catalysis cycle.

pathway, the RMSD between our simulated ADP-bound $A^t$ state (relaxed with an additional 100 ns of MD) with that of the ATP-binding dwell 5KNB is ∼1.5 Å (Figure S3).

Free-energy profiles along both pathways have comparable local energy barriers of height 6−7 kcal/mol for initial product release (Figure S7). However, the inward release pathway has a number of unbinding intermediates (Figure 5 and Movie S1), which are missing from the outward release mechanism. The transient trapping of $P_i$ in these intermediates suggests that, in the solvated protein environment, the inward release path out of the ATPase motor can be slower than the outward release mechanism, which we examine using the 2D free-energy profiles and Brownian dynamics or BD simulations (see the Methods section). Stochastic sampling of the outward path using BD reveals that a 20 Å long displacement of the $P_i$ from the binding site into the bulk solvent takes an estimated time of 4.2 ± 2.2 $\mu$s. In comparison, displacement of the $P_i$ by 15 Å from the catalytic site along the inward release pathway requires 65.9 ± 29.3 $\mu$s (Figure S7). The inward pathway requires lesser rearrangement of the product-containing AB interface than the outer one, thus allowing for a small aperture for rapid $P_i$ release from the pocket. However, the $P_i$ still remains nonspecifically bound to parts of the stalk−A interface. This result of incomplete $P_i$ unbinding finds support from the experimental observation of "noncatalytic" phosphate binding sites in F-type ATP synthase, also somewhere in the A-subunit.[49] Nucleotide binding to these sites is expected to play a regulatory role.[50] Though the exact locations of the noncatalytic $P_i$ sites are yet unknown, our simulation now shows the possibility of electrostatically driven secondary $P_i$ binding in V-ATPase, beyond the primary ATP site and traditional $P_i$-binding loop (Movie S1 and Figure S8). Two more repeats of the metadynamics along the inward path reproduced a similar observation.

We note that this analysis is semiquantitative, given that the BD treatment of a low-dimensional energy profile misses the contributions of alternate pathways and hidden barriers on the rate, especially when the profile does not necessarily guarantee a minimum free-energy pathway. However, the barriers seen in the metadynamics simulations, despite reflecting our bias on the choice of displacement-based reaction coordinates, remain well within 13 kcal/mol—an upper bound of energy barriers for molecular dynamics within ATP motors set by the net energy released from ATP hydrolysis.[9] These values are also comparable to the ones reported for F-type ATPase in ref 18. Thus, inferring from the BD trajectories of a probe particle across multiple barriers of heights 6−7 kcal/mol, we attribute within errors the lifetime of the product release dwell to be in the sub-millisecond regime, which enables the diffusion of $P_i$ out of the ATP pocket. Driving the $P_i$ further, i.e., completely out of the protein via the inward path, can take even longer, making it computationally more expensive to model. Taken together, our comparison of the rates suggests that $P_i$ unbinds before ADP (Figure S5), and the duration of the $P_i$-release dwell will be controlled by the kinetics of the inward release pathway. Approximately 10-fold slower than the outer pathway, this inner route of $P_i$ unbinding still remains thermodynamically accessible on the 30−100 $\mu$s time scales and will offer a bottleneck for ATP activity by the V-type motor. Noting that single-molecule experiments have now reached the time resolution of microseconds only very recently,[8] it is expected that this new dwell can also be seen in future experiments.

A transfer entropy or so-called mutual information analysis (see the Methods section) along the inward pathway further


https://doi.org/10.1021/acscentsci.1c01599
ACS Cent. Sci. 2022, 8, 915−925

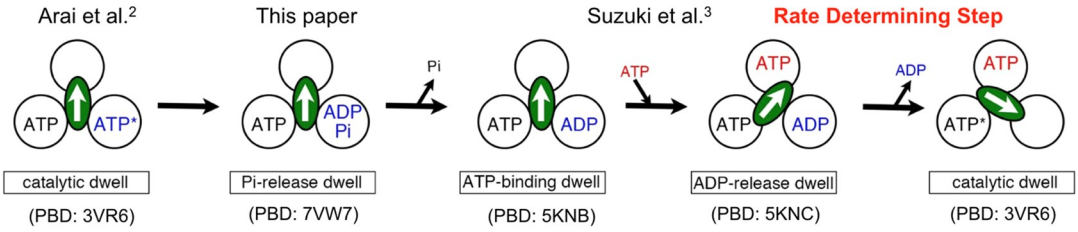


**Figure 7.** Coupling scheme for ATP hydrolysis of *E. hirae* $V_1$-ATPase. Each cycle in the figure represents the chemical state of the nucleotide-binding site from the cytoplasmic side. The central arrows in the ellipses represent the orientation of the central axis beginning from the 12 o'clock position, which corresponds to the catalytic dwell. ATP* represents an ATP molecule that is committed to hydrolysis. We have identified the final, ADP-release step as rate-limiting. See the text for additional details.

reveals that information is exchanged between the backbone RMSD of the AB binding interface residues and the reaction coordinate vector of the product release (Figure S9).[30] In particular, coupling of the Arg finger R350 conformations and the residues in its vicinity with the hinge movements of the ADP·$P_i$-bound $B^t$-subunit is roughly 2-fold more pronounced than the coupling between any other B-subunit residues with the global interface changes. This correlation between local and global changes mediated specifically by R350 decreases from the $B^t$ to $B^b$ to $B^e$ conformations. Based on this systematic difference in side chain information between the $B^t$ and $B^e$ sites, it is inferred that disengagement of the $P_i$ from R350 will break the correlation between local and global conformations of the B-subunit. Since the breaking of such information channels is energetically expensive,[31] the unbinding of $P_i$ from the Arg finger is expected to offer a rate-determining barrier for the transformation of the $P_i$-release dwell into the ATP-binding dwell.

According to Boyer's "binding change" model in the hydrolysis direction, any of the three catalytic sites on the enzyme first unbind ADP and/or phosphate in sequence and, second, undergo a conformational change so as to intake and subsequently bind a new ATP.[9] Akin to the first step of this model, originally proposed for F-type ATPases, our results now show that, even in the $V_1$ motor, the enzyme unbinds phosphate and ADP in a sequence from the $A^t$ sight, and not simultaneously. Next, to complete the second step of Boyer's model for V-type ATPase, i.e., to move from the $P_i$-release dwell to the ATP-binding dwell of Figure 3, it is necessary that information is transferred from the $A^t$ site to the $A^e$ site so a new ATP can enter the motor from the *e* site after the product is released from the *t* site. However, such information exchange between local ligand changes and global conformational changes (*ala* induced fit) is less feasible at the $A^e$ site, where neither ATP nor ADP·$P_i$ binding is significant.[2] Thus, we probe protein−protein interface changes between the neighboring 120° apart *t* and *e* sites to elucidate how product release enables new reactant entry.

After phosphate release, we find that the interaction between the $A^t$ and the central stalk loosens, making the stalk more flexible. This additional mobility of the stalk also alleviates its interactions with the $A^e$ and $B^e$ (Figure 6). Consequently, the solvent-accessible surface area of the $A^e$ pocket increases by ∼25%, allowing space for potential entry of a new ATP and completing the $P_i$-release dwell → ATP-binding dwell transition. The flexibility of the central stalk has been an issue of major contention in the F-ATPase area. While the crystallographers found no evidence of a deformed stalk in the molecular models, the single-molecule imaging and computational studies found evidence of a spatially dependent elastic modulus of the stalk[32] in the $F_1$ motor, indicating flexibility and potential deformation of the stalk during rotation. The central stalk of the $V_1$-ATPase was already crystallographically shown to be deformed.[5] Here, we find a design advantage of such stalk mobility that allows information transfer between $P_i$ release from the *tight* pocket and reactant entry in the neighboring *empty* pocket.

## DISCUSSION

Almost four decades after Boyer and Walker's proposal of a rotatory catalysis mechanism in ATPases, we are still in the middle of molecular biophysics investigations resolving the details of the ATP activity.[33] Static snapshots determined using X-ray crystallography and MD simulation pictures of the $V_1$ rotary motor from *E. hirae* are presented and compared in the schematic of Figure 7. Simulation studies provide a complementary view of the rotation and ATP hydrolysis, by connecting the static intermediate structures during rotation. We had already established that after the *empty* form (in the catalytic dwell) changes to the *bindable* form (in the ATP-binding dwell), new ATP is bound to induce further conformational changes to drive the central stalk rotation, which appears to undergo a wringing movement during rotation to reset back to a new catalytic dwell.[25] The time scale of the rotation of the central stalk was determined to be of the order of 1.4 ms, but only after both the ADP and $P_i$ were released from the *tight* pocket.

Here, we focus specifically on the V-ATPase's product-release process. We find that the unique asymmetry of the $A_3B_3$ ring with three identical AB pairs facilitates $P_i$ release and the introduction of a new ATP into the hexameric motor prior to this stalk rotation. The ATP hydrolysis intermediate, which is trapped here using ADP·$AlF_4^-$, spontaneously relaxes an $A^t$ pocket to a marginally open conformation creating a $P_i$-release dwell. This new intermediate in turn facilitates the formation of a small aperture for releasing the $P_i$ either internally toward or away from the stalk. Residues required for the ATP binding and hydrolysis are also the ones found responsible for coupling the $P_i$-induced binding pocket reorganization with larger-scale conformational transformations of the A-subunits. In particular, disengagement of $P_i$ from the Arg350 finger residue is deemed a rate-determining step of the product release process. Noting that the Arginine finger is ubiquitous across many AAA + ATP-hydrolyzing motors that use the so-called Walker motif,[34] the $P_i$-release mechanism presented here is generalizable to these systems.

The ADP-bound conformation formed after the $P_i$ reduces the stalk−A-subunit interaction, opening up a neighboring AB interface for accepting a new ATP. Through molecular simulations, we find how the two ATP/ADP·$P_i$-sites


https://doi.org/10.1021/acscentsci.1c01599
ACS Cent. Sci. 2022, 8, 915−925

communicate with each other for synchronizing the protein conformations necessary for product release with the ones needed for ATP entry. Evidence of such multisite conformational allostery was not included in the original binding-change model. Therefore, our joint structure-determination and computational work brings to light how the cooperativity between the AB proteins works inside a hexameric architecture to connect the $P_i$-release dwell with the ATP-binding dwell.

Finally, comparing all of the available kinetic data, we note that the ATP-binding event and a 120° rotation back to the catalytic dwell takes ∼1.4 ms,[25] which is slower than the cumulative time of the spontaneous catalytic dwell → $P_i$-release dwell transition that takes <500 ns of MD, and $P_i$-release → ATP-binding dwell transition that takes at least between 30 and 100 μs of BD following the inward release path (Figure S7K). The $P_i$ exit outward from the central stalk is even ∼10-fold faster taking 2−6 μs of BD. It is worth noting that errors in these computational rate estimates can arise from a number of factors including the choice of collective variables for metadynamics simulations of $P_i$ unbinding, convergence of free-energy profiles due to computational time limitations, or the size of the BD time steps. Nonetheless, the stated kinetic trend will still hold even if we assume that the current rate estimates of $P_i$ release are within an order of magnitude of uncertainty. Thus, given that the turnover time of $V_1$ in the hydrolysis direction is within ∼100 $s^{-1}$, the only remaining molecular events that can be attributed to be the slowest along the entire rotary-catalysis cycle is associated with ADP unbinding dwell. Since ATP entry to a *bindable* pocket is spontaneous, through inspection of all of the steps, we can now pinpoint that ADP-release is the rate-limiting step of $V_1$-ATPase turnover. This finding is in line with single-molecule experiments that have implicated ADP accumulation and inhibition as the central cause for stoppage in the rotatory movement of V-type motors.[8,35] Now, our proposed mechanism of rotary-catalysis brings to light the molecular origins of the inhibition as well as activity of $V_1$-ATPase.

## METHODS

**Protein Preparation.** The $A_3B_3$ and DF complexes were expressed in an *Escherichia coli* system, as described previously.[36] This system employs a mixture of plasmids containing the corresponding genes. $A_3B_3$DF complex ($EhV_1$) was reconstituted and purified as follows:[37] purified $A_3B_3$ and DF complexes in buffer A [20 mM Tris-HCl, 150 mM NaCl, and 2 mM dithiothreitol (DTT); pH 8.0] were mixed in a 1:4 molar ratio with the addition of MES (100 mM final concentration; pH 6.0) with 5 mM ADP and 5 mM $MgSO_4$. After 1 h, $AlCl_3$ (1 mM final concentration) and NaF (5 mM final concentration) were added and incubated for 30 min at room temperature. $V_1$-ATPase was purified using a Superdex 200 10/300 GL (GE Healthcare) column equilibrated with buffer B (20 mM MES, 10% glycerol, 100 mM NaCl, 5 mM $MgSO_4$, and 2 mM DTT; pH 6.5). Purified complex was concentrated with an Amicon Ultra 30 K unit (Merck Millipore).

**Measurement of ATP Activity.** ATP hydrolysis activities of the $EhV_1$ were measured using an ATP regenerating system.[2,3] ATP hydrolysis rates were determined in terms of the rate of NADH oxidation, which was measured for 1 min as a decrease in absorbance of 340 nm at room temperature, and the measurement was repeated three times. Protein concentrations were determined using the Pierce BCA protein assay kit (Thermo Fisher Scientific) with bovine serum albumin as the standard.

**Protein Crystallization and Structure Determination.** Crystals of $EhV_1$ were obtained by mixing 0.5 μL of purified protein solution (17 mg $mL^{-1}$ protein in buffer B) with 0.5 μL of reservoir solution (0.1 M bis-tris propane, 0.2 M NaF, 20.8% PEG-3350; pH 6.5), using the sitting-drop vapor diffusion method at 296 K. Crystals were soaked in the solution (0.1 M bis-tris propane, 21% PEG-3350, 5 mM ADP, 1 mM $AlCl_3$, 5 mM NaF, 3 mM $MgCl_2$, 0.28 M NaCl, and 20% glycerol; pH 6.5) for 1 min, mounted on cryoloops (Hampton Research, Aliso Viejo, CA), flash-cooled, and stored in liquid nitrogen.

The X-ray diffraction data were collected from a single crystal at a cryogenic temperature (100 K) on BL-17A ($\lambda$ = 0.9800 Å) at the Photon Factory (Tsukuba, Japan). The collected data were processed using XDS[38] software. The structure was solved by molecular replacement with Phaser[39] as a search model for nucleotide-free $V_1$-ATPase (PDB: 3VR5). The atomic model was built using Coot[40] and iteratively refined using Phenix[41] and REFMAC5.[42] TLS (Translation/Libration/Screw) refinement was performed in late stages of refinement. The refined structures were validated with RAMPAGE.[43] All molecular graphics were prepared using PyMOL (The PyMOL Molecular Graphics System, Version 2.1.1, Schrodinger, LLC, New York, NY).

**Molecular Dynamics Simulations.** The MD study is based on a crystal structure of the $V_1$-rotor from *Enterococcus hirae* (PDB: 3VR6).[2] For simulation purposes, the artificial ATP mimetics, namely, AMP·PNP, which are employed as inhibitors for isolating crystals, are replaced by real ATP molecules in the bound states (*b*) and ADP and an inorganic phosphate or $P_i$ (modeled as $H_2PO_4^-$) in the tight state (*t*) (see Figure 2). Structural analyses[2] have demonstrated that nonhydrolyzable AMP·PNP can successfully mimic the ATP and ADP + $P_i$ binding states in $F_1$-ATPase; different ATP analogues produced, in fact, similar binding conformations.[27] The simulation was performed for the entire $V_1$-rotor.

The $V_1$-rotor is solvated in a water box of size 170 × 170 × 190 $Å^3$ with 150 mM NaCl; the simulation system size is 0.49 M atoms. This structure was solvated and ionized in VMD, wherein 168 273 water molecules were added. After a 4000-step energy minimization, the system is thermalized to 300 K in 50 ps at 1 atm, employing harmonic positional restraints with a 1 kcal/(mol $Å^2$) spring constant on heavy atoms. Keeping the same spring constant, a 1 ns equilibration in the isobaric−isothermal ensemble (1 atm at 300 K) is carried out, followed by a 4 ns canonical-ensemble simulation, gradually decreasing the spring constant to zero during the latter stage. All MD simulations in our study are performed using NAMD 2.14[44] with the CHARMM36 force field with correction for overcompensation for left-handed helix and CMAP corrections. The CHARMM-compatible $P_i$ force field parameters were developed and used by us in previous studies.[23]

**REST2 Simulations.** The initial structure of ATP-synthase was obtained from the $AlF_4$-bound crystal structure [resembling intermediate 1′ of the ADP·$P_i$-bound state (Figure S4), previously determined using MD simulations[25]]. This structure was then minimized, heated to 300 K, and equilibrated for 5 ns. REST2 simulation was performed using 32 replicas scanning a temperature range 300−3000 K, where the ADP·$P_i$ was defined as the solute. Each of the 32 REST2 replicas was simulated for 16 ns to attain a steady exchange-rate of 40−80% (Figure S6).


https://doi.org/10.1021/acscentsci.1c01599
ACS Cent. Sci. 2022, 8, 915−925

**Funnel Metadynamics and Free-Energy Computations.** In order to accelerate the unbinding/binding of $P_i$, well-tempered Funnel-metadynamics (FM)[29] was performed for 2000 and 400 ns for dissociation away from or toward the stalk. The FM simulations were performed in an NVT ensemble using the BioSimspace implementation in OpenMM. Following the OpenMM flavor of FM, a history-dependent bias was applied on two orthogonal CVs, namely, projection and extension, that define the funnel potential. The projection CV which is collinear to the funnel axis is defined by a vector connecting the center of mass Ca of ILE322, GLU261, and ASP 329 (Po) and GLU126, GLU275, and ASP364 (Px) for dissociation away from the stalk and GLY353 and PRO 268 for dissociation toward the stalk. The extension CV, on the other hand, is orthogonal to the projection CV and is restrained by a sigmoidal restraint function defined as follows:

$$S = h\left(\frac{1}{1 + e^{i(b-x)}}\right) + f \tag{1}$$

The parameters used to define the sigmoidal restraints are described in Table S2. For the FM, Gaussians hills with an initial height of 0.6 KJ $mol^{-1}$ was applied every ps, scaled by a WT scheme using a bias factor of 30. The hill widths chosen for the projection and extension CVs are 0.25 and 0.3 Å, respectively.

**Brownian Dynamics.** BD simulations were employed to model the diffusion of a probe particle on the 2-dimensional free-energy profile determined using the funnel metadynamics simulation. These computations were performed on GPU-accelerated Atomic-Resolution Brownian Dynamics (ARBD) software[45] using our established protocols.[46−48] First, a probe particle is defined with the diffusion coefficient of 1.5 $Å^2$/ns and 5.10 $Å^2$/ns for dissociation toward and away from the stalk on the basis of a previous diffusion calculation of $P_i$ by Okazaki et al.[18] Second, the product-release landscape was projected on a 2D grid with the same spacing as that of the original PMFs. Third, using gradients of this profile and the stated diffusion coefficient, the equation of motion is integrated over a time step of 1 ps (for the more rugged inward release) and 3 ps (for the less rugged outward release). Each simulation was repeated 100 times, stating from random initial positions on the free-energy landscape. We monitor the average time taken by the diffusive particle to exit the binding pocket and reach either in the bulk solvent (20 Å along the funnel axis on the outward pathway) or the stalk−A-subunit interface (15−16 Å along the funnel axis on the inward pathway). Distribution of these transition times is presented in Figure S7I−K, where we also compare the timing with that of a random walker on a flat landscape with diffusion coefficient identical to $P_i$. Finally, noting that the 2D energy surfaces converge with numerical errors of 1−2 kcal/mol after an almost 1 $\mu$s metadynamics simulation (see the 1D profiles of Figure S7), the BD simulations for the outward path were repeated with three different surfaces derived from the last 150 ns of metadynamics, saved at increments of 50 ns. The transition times on the corresponding surfaces are computed with BD, and their distribution is presented in Figure S7J. A reasonable agreement between these distributions suggests that the uncertainty in transition-time estimates arising due to the numerical errors on the surfaces is lesser than that due to thermal fluctuations at room temperature.

**Allosteric Network Analysis.** The allosteric network analysis was performed with the NetworkView tool on VMD. The final 100 ns of the MD trajectories was strided by a factor of 10, creating nearly 1000 frames. These frames were analyzed by CARMA to create a covariance matrix, following which the allosteric networks are created at the $C_\alpha$-level of detail, and the community substructures are analyzed using the Girvan−Newman method and default NetworkView parameters on VMD. Edges are drawn between nodes whose residues are within a cutoff distance of 4.5 Å for at least 75% of an MD trajectory.

**Mutual Information Analysis.** Given two random variables $X$ and $Y$, mutual information is an information theory metric that quantifies the interdependence between $X$ and $Y$ in terms of correlation (and not directionality). Mutual information (MI) is commonly expressed as

$$\mathrm{MI}(X, Y) = \int P(X, Y) \ln \frac{P(X, Y)}{P(X)\,P(Y)} \mathrm{d}X\,\mathrm{d}Y \tag{2}$$

Here, $P(X, Y)$ is the joint probability distribution of $X$ and $Y$ and $P(X)$ and $P(Y)$ are their respective marginals. In order to understand the correlation between protein dynamics and ligand release, MI was computed between the RMSD of protein backbone and the position of $P_i$ along the release pathway. In this case, $P(X, Y)$ is the joint probability distribution of RMSD of the protein backbone and the position of the ligand along the release pathway. We have in-house code to perform this analysis.

## ■ ASSOCIATED CONTENT

### Supporting Information

The Supporting Information is available free of charge at https://pubs.acs.org/doi/10.1021/acscentsci.1c01599.

Movie S1: Funnel metadynamics trajectory of the inward release pathway of $P_i$ starting from the $P_i$-release dwell approaching the ATP-binding dwell; within our finite simulations, complete release of the $P_i$ from the ATPase is not observed, though disengagement from the ATP-binding pocket is apparent (MOV)

Movie S2: Same as Movie S1, but for the outward release pathway, wherein the $P_i$ after leaving the binding pocket completely disengages from the V1-ATPase (MOV)

Further theoretical details, including a detailed explanation of the exciting model of the rotation mechanism of *E. hirae* $V_1$-ATPase, supplemental *in silico* data, employed simulation parameters, and a summary of simulations performed (PDF)

Transparent Peer Review report available (PDF)

## ■ AUTHOR INFORMATION

### Corresponding Authors

**Takeshi Murata** − *Department of Chemistry, Graduate School of Science, Chiba University, Inage, Chiba 263-8522, Japan; Membrane Protein Research and Molecular Chirality Research Centers, Chiba University, Inage, Chiba 263-8522, Japan; Structure Biology Research Center, Institute of Materials Structure Science, High Energy Accelerator Research Organization (KEK), Ibaraki 305-0801, Japan*; Email: t.murata@faculty.chiba-u.jp

**Abhishek Singharoy** − *School of Molecular Sciences, Arizona State University, Tempe, Arizona 85281, United States;*



https://doi.org/10.1021/acscentsci.1c01599
ACS Cent. Sci. 2022, 8, 915−925

orcid.org/0000-0002-9000-2397; Email: asinghar@asu.edu

### Authors

**Mrinal Shekhar** − *Center for Development of Therapeutics, Broad Institute of MIT and Harvard, Cambridge, Massachusetts 02142, United States*

**Chitrak Gupta** − *School of Molecular Sciences, Arizona State University, Tempe, Arizona 85281, United States*

**Kano Suzuki** − *Department of Chemistry, Graduate School of Science, Chiba University, Inage, Chiba 263-8522, Japan*

**Chun Kit Chan** − *School of Molecular Sciences, Arizona State University, Tempe, Arizona 85281, United States*

Complete contact information is available at: https://pubs.acs.org/10.1021/acscentsci.1c01599

### Author Contributions

#M.S., C.G., and K.S. contributed equally to this work.

### Notes

The authors declare no competing financial interest.

*Data Availability*. The atomic coordinates and structure factors of $2_{(ADP\cdot AlF4)}V_1$ have been deposited in the Protein Data Bank under the accession code 7VW7.

## ■ ACKNOWLEDGMENTS

The synchrotron radiation experiments were performed at Photon Factory (proposals 2012G-132). We thank the beamline staff at BL1A and BL17A of Photon Factory (Tsukuba, Japan) for help during data collection. This research was supported in part by the Japan Agency for Medical Research and Development (AMED) under Grants 21fk0108092, JP21am0101083, and JP22ama121013 (to T.M.) and by a Grant-in-Aid for Scientific Research from Japan Society for the Promotion of Science (JSPS) under Grants 18H05425 and 21H02409 (to T.M.). A.S. acknowledges the CAREER award from NSF (MCB-1942763). This work used the Extreme Science and Engineering Discovery Environment (XSEDE), which is supported by National Science Foundation grant number ACI-1548562, and Oak Ridge Leadership Computing Facility, supported by the Office of Science, Department of Energy (DE-AC05-00OR22725).

## ■ REFERENCES

(1) Forgac, M. Vacuolar ATPases: Rotary Proton Pumps in Physiology and Pathophysiology. *Nat. Rev. Mol. Cell Biol.* **2007**, *8* (11), 917−929.

(2) Arai, S.; Saijo, S.; Suzuki, K.; Mizutani, K.; Kakinuma, Y.; Ishizuka-Katsura, Y.; Ohsawa, N.; Terada, T.; Shirouzu, M.; Yokoyama, S.; Iwata, S.; Yamato, I.; Murata, T. Rotation Mechanism of Enterococcus Hirae V1-ATPase Based on Asymmetric Crystal Structures. *Nature* **2013**, *493* (7434), 703−707.

(3) Suzuki, K.; Mizutani, K.; Maruyama, S.; Shimono, K.; Imai, F. L.; Muneyuki, E.; Kakinuma, Y.; Ishizuka-Katsura, Y.; Shirouzu, M.; Yokoyama, S.; Yamato, I.; Murata, T. Crystal Structures of the ATP-Binding and ADP-Release Dwells of the $V_1$ Rotary Motor. *Nat. Commun.* **2016**, *7*, 13235.

(4) Maruyama, S.; Suzuki, K.; Imamura, M.; Sasaki, H.; Matsunami, H.; Mizutani, K.; Saito, Y.; Imai, F. L.; Ishizuka-Katsura, Y.; Kimura-Someya, T.; Shirouzu, M.; Uchihashi, T.; Ando, T.; Yamato, I.; Murata, T. Metastable Asymmetrical Structure of a Shaftless V1Motor. *Sci. Adv.* **2019**, *5* (1), No. eaau8149.

(5) Saijo, S.; Arai, S.; Hossain, K. M. M.; Yamato, I.; Suzuki, K.; Kakinuma, Y.; Ishizuka-Katsura, Y.; Ohsawa, N.; Terada, T.; Shirouzu, M.; Yokoyama, S.; Iwata, S.; Murata, T. Crystal Structure of the Central Axis DF Complex of the Prokaryotic V-ATPase. *Proc. Natl. Acad. Sci. U. S. A.* **2011**, *108* (50), 19955−19960.

(6) Murata, T.; Yamato, I.; Kakinuma, Y.; Leslie, A. G. W.; Walker, J. E. Structure of the Rotor of the V-Type Na+-ATPase from Enterococcus Hirae. *Science* **2005**, *308* (5722), 654−659.

(7) Murata, T.; Yamato, I.; Kakinuma, Y. Structure and Mechanism of Vacuolar Na+-Translocating ATPase From Enterococcus Hirae. *J. Bioenerg. Biomembr.* **2005**, *37* (6), 411−413.

(8) Iida, T.; Minagawa, Y.; Ueno, H.; Kawai, F.; Murata, T.; Iino, R. Single-Molecule Analysis Reveals Rotational Substeps and Chemo-Mechanical Coupling Scheme of Enterococcus Hirae V1-ATPase. *J. Biol. Chem.* **2019**, *294* (45), 17017−17030.

(9) Boyer, P. D. The Binding Change Mechanism for ATP Synthase — Some Probabilities and Possibilities. *Biochim. Biophys. Acta BBA - Bioenerg.* **1993**, *1140* (3), 215−250.

(10) Walker, J. E. The ATP Synthase: The Understood, the Uncertain and the Unknown. *Biochem. Soc. Trans.* **2013**, *41* (1), 1−16.

(11) Abrahams, J. P.; Leslie, A. G. W.; Lutter, R.; Walker, J. E. Structure at 2.8 Å Resolution of F 1 -ATPase from Bovine Heart Mitochondria. *Nature* **1994**, *370* (6491), 621.

(12) Menz, R. I.; Walker, J. E.; Leslie, A. G. W. Structure of Bovine Mitochondrial F1-ATPase with Nucleotide Bound to All Three Catalytic Sites: Implications for the Mechanism of Rotary Catalysis. *Cell* **2001**, *106* (3), 331−341.

(13) Kagawa, R.; Montgomery, M. G.; Braig, K.; Leslie, A. G. W.; Walker, J. E. The Structure of Bovine F1-ATPase Inhibited by ADP and Beryllium Fluoride. *EMBO J.* **2004**, *23* (14), 2734−2744.

(14) Rees, D. M.; Montgomery, M. G.; Leslie, A. G. W.; Walker, J. E. Structural Evidence of a New Catalytic Intermediate in the Pathway of ATP Hydrolysis by F1-ATPase from Bovine Heart Mitochondria. *Proc. Natl. Acad. Sci. U. S. A.* **2012**, *109* (28), 11139−11143.

(15) Gledhill, J. R.; Montgomery, M. G.; Leslie, A. G. W.; Walker, J. E. How the Regulatory Protein, IF1, Inhibits F1-ATPase from Bovine Mitochondria. *Proc. Natl. Acad. Sci. U. S. A.* **2007**, *104* (40), 15671−15676.

(16) Senior, A. E. ATP Synthesis by Oxidative Phosphorylation. *Physiol. Rev.* **1988**, *68* (1), 177−231.

(17) Noji, H.; Yasuda, R.; Yoshida, M.; Kinosita, K. Direct Observation of the Rotation of F1-ATPase. *Nature* **1997**, *386* (6622), 299−302.

(18) Okazaki, K.; Hummer, G. Phosphate Release Coupled to Rotary Motion of F1-ATPase. *Proc. Natl. Acad. Sci. U. S. A.* **2013**, *110* (41), 16468−16473.

(19) Czub, J.; Wieczór, M.; Prokopowicz, B.; Grubmüller, H. Mechanochemical Energy Transduction during the Main Rotary Step in the Synthesis Cycle of F1-ATPase. *J. Am. Chem. Soc.* **2017**, *139* (11), 4025−4034.

(20) Ekimoto, T.; Ikeguchi, M. Multiscale Molecular Dynamics Simulations of Rotary Motor Proteins. *Biophys. Rev.* **2018**, *10* (2), 605−615.

(21) Stewart, A. G.; Laming, E. M.; Sobti, M.; Stock, D. Rotary ATPases—Dynamic Molecular Machines. *Curr. Opin. Struct. Biol.* **2014**, *25*, 40−48.

(22) Singharoy, A.; Chipot, C.; Ekimoto, T.; Suzuki, K.; Ikeguchi, M.; Yamato, I.; Murata, T. Rotational Mechanism Model of the Bacterial V1Motor Based on Structural and Computational Analyses. *Front. Physiol.* **2019**, *10*, 46.

(23) Ma, W.; Schulten, K. Mechanism of Substrate Translocation by a Ring-Shaped ATPase Motor at Millisecond Resolution. *J. Am. Chem. Soc.* **2015**, *137* (8), 3031−3040.

(24) Fisher, A. J.; Smith, C. A.; Thoden, J.; Smith, R.; Sutoh, K.; Holden, H. M.; Rayment, I. X-Ray Structures of the Myosin Motor Domain of Dictyostelium Discoideum Complexed with MgADP.Cntdot.BeFx and MgADP.Cntdot.AlF4-. *Biochemistry* **1995**, *34* (28), 8960−8972.

(25) Singharoy, A.; Chipot, C.; Moradi, M.; Schulten, K. Chemomechanical Coupling in Hexameric Protein-Protein Interfaces

Harnesses Energy within V-Type ATPases. *J. Am. Chem. Soc.* **2017**, *139* (1), 293−310.
(26) Singharoy, A.; Chipot, C. Methodology for the Simulation of Molecular Motors at Different Scales. *J. Phys. Chem. B* **2017**, *121* (15), 3502−3514.
(27) Hong, S.; Pedersen, P. L. ATP Synthase and the Actions of Inhibitors Utilized To Study Its Roles in Human Health, Disease, and Other Scientific Areas. *Microbiol. Mol. Biol. Rev.* **2008**, *72* (4), 590−641.
(28) Nakamoto, R. K.; Baylis Scanlon, J. A.; Al-Shawi, M. K. The Rotary Mechanism of the ATP Synthase. *Arch. Biochem. Biophys.* **2008**, *476* (1), 43−50.
(29) Limongelli, V.; Bonomi, M.; Parrinello, M. Funnel Metadynamics as Accurate Binding Free-Energy Method. *Proc. Natl. Acad. Sci. U. S. A.* **2013**, *110*, 6358.
(30) Wang, Y.; Ribeiro, J. M. L.; Tiwary, P. Past-Future Information Bottleneck for Sampling Molecular Reaction Coordinate Simultaneously with Thermodynamics and Kinetics. *Nat. Commun.* **2019**, *10* (1), 3573.
(31) Schoeler, C.; Bernardi, R. C.; Malinowska, K. H.; Durner, E.; Ott, W.; Bayer, E. A.; Schulten, K.; Nash, M. A.; Gaub, H. E. Mapping Mechanical Force Propagation through Biomolecular Complexes. *Nano Lett.* **2015**, *15* (11), 7370−7376.
(32) Martin, J. L.; Ishmukhametov, R.; Spetzler, D.; Hornung, T.; Frasch, W. D. Elastic Coupling Power Stroke Mechanism of the F1-ATPase Molecular Motor. *Proc. Natl. Acad. Sci. U. S. A.* **2018**, *115* (22), 5750−5755.
(33) Dautant, A.; Meier, T.; Hahn, A.; Tribouillard-Tanvier, D.; di Rago, J.-P.; Kucharczyk, R. ATP Synthase Diseases of Mitochondrial Genetic Origin. *Front. Physiol.* **2018**, *9*, 329.
(34) delToro, D.; Ortiz, D.; Ordyan, M.; Sippy, J.; Oh, C.-S.; Keller, N.; Feiss, M.; Catalano, C. E.; Smith, D. E. Walker-A Motif Acts to Coordinate ATP Hydrolysis with Motor Output in Viral DNA Packaging. *J. Mol. Biol.* **2016**, *428* (13), 2709−2729.
(35) Toei, M.; Noji, H. Single-Molecule Analysis of F0F1-ATP Synthase Inhibited by N,N-Dicyclohexylcarbodiimide. *J. Biol. Chem.* **2013**, *288* (36), 25717−25726.
(36) Minagawa, Y.; Ueno, H.; Hara, M.; Ishizuka-Katsura, Y.; Ohsawa, N.; Terada, T.; Shirouzu, M.; Yokoyama, S.; Yamamoto, I.; Muneyuki, E.; Noji, H.; Murata, T.; Iino, R. Basic Properties of Rotatory Dynamics of the Moleculat Motor *Enterococcus hirae* $V_1$-ATPase. *J. Biol. Chem.* **2013**, *288*, 32700−32707.
(37) Arai, S.; Yamato, I.; Shiokawa, A.; Saijo, S.; Kakinuma, Y.; Ishizuka-Katsura, Y.; Toyama, M.; Terada, T.; Shirouzu, M.; Yokoyama, S.; Iwata, S.; Murata, T. Reconstitution in Vitro of the Catalytic Portion (NtpA3-B3-D-G Complex) of Enterococcus Hirae V-Type Na+-ATPase. *Biochem. Biophys. Res. Commun.* **2009**, *390* (3), 698−702.
(38) Kabsch, W. XDS. *Acta Crystallogr. D Biol. Crystallogr.* **2010**, *66* (2), 125−132.
(39) McCoy, A. J.; Grosse-Kunstleve, R. W.; Adams, P. D.; Winn, M. D.; Storoni, L. C.; Read, R. J. Phaser Crystallographic Software. *J. Appl. Crystallogr.* **2007**, *40* (4), 658−674.
(40) Emsley, P.; Cowtan, K. Coot: Model-Building Tools for Molecular Graphics. *Acta Crystallogr. D Biol. Crystallogr.* **2004**, *60* (12), 2126−2132.
(41) Adams, P. D.; Afonine, P. V.; Bunkóczi, G.; Chen, V. B.; Davis, I. W.; Echols, N.; Headd, J. J.; Hung, L.-W.; Kapral, G. J.; Grosse-Kunstleve, R. W.; McCoy, A. J.; Moriarty, N. W.; Oeffner, R.; Read, R. J.; Richardson, D. C.; Richardson, J. S.; Terwilliger, T. C.; Zwart, P. H. PHENIX: A Comprehensive Python-Based System for Macromolecular Structure Solution. *Acta Crystallogr. D Biol. Crystallogr.* **2010**, *66* (2), 213−221.
(42) Murshudov, G. N.; Vagin, A. A.; Dodson, E. J. Refinement of Macromolecular Structures by the Maximum-Likelihood Method. *Acta Crystallogr. D Biol. Crystallogr.* **1997**, *53* (3), 240−255.
(43) Lovell, S. C.; Davis, I. W.; Arendall III, W. B.; de Bakker, P. I. W.; Word, J. M.; Prisant, M. G.; Richardson, J. S.; Richardson, D. C. Structure validation by C$\alpha$ geometry: $\phi$,$\psi$ and C$\beta$ deviation. *Proteins Struct. Funct. Bioinforma.* **2003**, *50* (3), 437−450.
(44) Phillips, J. C.; Hardy, D. J.; Maia, J. D. C.; Stone, J. E.; Ribeiro, J. V.; Bernardi, R. C.; Buch, R.; Fiorin, G.; Hénin, J.; Jiang, W.; McGreevy, R.; Melo, M. C. R.; Radak, B. K.; Skeel, R. D.; Singharoy, A.; Wang, Y.; Roux, B.; Aksimentiev, A.; Luthey-Schulten, Z.; Kalé, L. V.; Schulten, K.; Chipot, C.; Tajkhorshid, E. Scalable Molecular Dynamics on CPU and GPU Architectures with NAMD. *J. Chem. Phys.* **2020**, *153* (4), 044130.
(45) Comer, J.; Aksimentiev, A. Predicting the DNA sequence dependence of nanopore ion current using atomic-resolution Brownian dynamics. *J. Phys. Chem. C* **2012**, *116*, 3376.
(46) Benson, C. R.; Maffeo, C.; Fatila, E.; Liu, Y.; Sheetz, E. G.; Aksimentiev, A.; Singharoy, A.; Flood, A. Inchworm movement of two rings switching onto a thread by biased Brownian diffusion represent a three-body problem. *Proc. Nat. Acad. Sci.* **2018**, *115* (38), 9391−9396.
(47) Singharoy, A.; Maffeo, C.; Delgado-Magnero, K. H.; Swainsbury, D. J. K.; Sener, M.; Kleinekathöfer, U.; Vant, J.; Nguyen, J.; Hitchcock, A.; Isralewitz, B.; Teo, I.; Chandler, D.; Stone, J.; Phillips, J.; Pogorelov, T.; Mallus, M.; Chipot, C.; Luthey-Schulten, Z.; Tieleman, P.; Hunter, C. N.; Tajkhorshid, E.; Aksimentiev, A.; Schulten, K. Atoms to phenotypes: molecular design principles of cellular energy metabolism. *Cell* **2019**, *179* (5), 1098−1111.
(48) Chan, C. K.; Singharoy, A.; Tajkhorshid, E. Anionic Lipids Confine Cytochrome c2 to the Surface of Bioenergetic Membranes without Compromising Its Interaction with Redox Partners. *Biochemistry* **2022**, *61* (5), 385−397.
(49) Beharry, S.; Bragg, P. D. Properties of bound in organic phosphate on bovine mitochondrial FoF1 ATP synthase. *J. Bioenerg. Biomembr.* **2001**, *33* (1), 35−45.
(50) Bald, D.; Amano, T.; Muneyuki, E.; Pitard, B.; Rigaud, J.; Kruip, J.; Hisabori, T.; Yoshidai, M.; Shibata, M. ATP Synthesis by F0F1-ATP Synthase Independent of Noncatalytic Nucleotide Binding Sites and Insensitive to Azide Inhibition. *J. Biol. Chem.* **1998**, *273* (2), 865−870.


https://doi.org/10.1021/acscentsci.1c01599
*ACS Cent. Sci.* 2022, 8, 915−925